



Research paper

Neural network-assisted sensitivity analysis applied to finite-element simulations of plant-fiber microdroplet tests

Valentin Senk¹*, Markus Königsberger¹, Sebastian Pech¹, Josef Füssl¹*Institute of Mechanics of Materials and Structures, Vienna University of Technology, Karlsplatz 13/202, 1040, Vienna, Austria*

ARTICLE INFO

Keywords:

Microbond simulations
Finite element analysis (FEA)
Interfacial characterization
Surrogate modeling
Sensitivity analysis

ABSTRACT

Microdroplet tests are widely used for interface characterization in fiber-reinforced composites. However, their interpretation remains challenging due to complex, non-uniform stress states and the interplay of multiple geometric and mechanical factors. These challenges are further amplified in biocomposites, where natural fibers introduce additional variability in shape, orientation, and adhesion quality. This study presents a surrogate-based methodology to systematically quantify these sensitivities. A fully parameterized finite element model captures the geometric and interfacial complexities of natural fiber microdroplet tests. To efficiently explore parameter dependencies, a surrogate model based on artificial neural networks (ANNs) is trained on a comprehensive dataset of finite element simulations. Sensitivity analyses reveal strong effects of geometrical variability and mixed-mode behavior, questioning the validity of the commonly used scalar strength metric—interfacial shear strength (IFSS). By leveraging first- and second-order sensitivity analyses, we demonstrate how non-linear parameter interactions shape the macroscopic stress–displacement curves. These findings open up the possibility of using the surrogate model for inverse identification of interfacial parameters for use in composite-scale models, reducing reliance on repeated finite element simulations that often accompany interface characterization experiments.

1. Introduction

The characterization of fiber–matrix interfaces is critical for predicting and optimizing the performance of fiber-reinforced composites, as the interface governs load transfer, failure mechanisms, and long-term durability (Huang et al., 2021; Senk et al., 2025). Microdroplet tests, also known as microbond tests (Miller et al., 1987), are the most widely used technique for characterizing the interface quantitatively. In these tests, one or several resin droplets are deposited onto a single fiber, cured, and thereafter sheared off using parallel blades, with the load–displacement data recorded. Traditionally, these tests are evaluated by dividing the maximum force by the embedded area (the contact area between fiber and droplet), providing access to the interfacial shear strength (IFSS) (Miller et al., 1987; Wagner et al., 1993; Craven et al., 2000).

Since stress states within the droplet and at the fiber–matrix interface are highly non-uniform (Herrera-Franco and Drzal, 1992; Herrera-Franco et al., 1992; Bannister et al., 1995; Pisanova et al., 2001; Ash et al., 2003) and characterized by a combination of shear and normal stresses at the interface (mixed-mode loading) (Minnicino and Santare, 2012), the IFSS is often a rigorous oversimplification. Rather, the

interface stresses are influenced by the droplet's geometry, the meniscus formation, and the blade position (also referred to as microvoid opening) (Chou et al., 1994; Pisanova et al., 2001; Ash et al., 2003; Kang et al., 2009). Additionally, the scatter of test results is generally high (Laurikainen et al., 2020), further complicating the reliable interpretation of interfacial properties. These challenges are further amplified when testing biocomposites, where natural fibers introduce additional complexity, such as anisotropy, non-circular and variable cross-sections, internal voids (lumen), and significant geometric variability (Baley et al., 2020). As biocomposites gain increasing attention for their environmental benefits, addressing these nuances is essential for ensuring a reliable characterization of interfacial properties.

Although the IFSS provides a convenient metric for characterizing interfacial adhesion, a single scalar strength measure cannot characterize the interfacial failure mechanisms sufficiently. Models that accurately predict the structural performance of composites (Ahmadian et al., 2019; Shu and Stanciulescu, 2023; Senk et al., 2025) typically adopt nonlinear traction–separation laws at the interface for shear and potentially for tensile failure. Neglecting interfacial nonlinearities in mesoscale models in turn oversimplifies interfacial behavior, reducing predictive accuracy and limiting practical applicability. Rather

* Corresponding author.

E-mail address: valentin.senk@tuwien.ac.at (V. Senk).<https://doi.org/10.1016/j.mechmat.2026.105689>

Received 15 January 2026; Received in revised form 12 March 2026; Accepted 2 April 2026

Available online 20 April 2026

0167-6636/© 2026 The Authors. Published by Elsevier Ltd. This is an open access article under the CC BY license (<http://creativecommons.org/licenses/by/4.0/>).

than calibrating the parameters, including fracture energies and shear-tension interaction, of these traction–separation laws such that the mesoscale model fits the experimentally measured composite behavior, interfacial tests should directly provide them. Despite the advance in testing practices (Dsouza et al., 2020) and considerable simulation efforts to gain insights into interfacial stresses and failure mechanisms of tests (Schüller et al., 1998; Ash et al., 2003; Pandey et al., 2012; Sockalingam et al., 2014; Dsouza et al., 2023) – see Section 2.1 for a comprehensive review – it remains an open question until today, if and how microdroplet tests results can be properly evaluated and ultimately translated to mesoscale failure predictions for biocomposites.

The main goal of this paper is to establish a quantitative link between experimentally measured force–displacement curves obtained from microdroplet tests and the interfacial traction–separation law governing fiber–matrix failure. Instead of relying on simplified scalar measures such as the interfacial shear strength (IFSS), the aim is to extract the underlying interfacial constitutive behavior responsible for mixed-mode debonding.

Achieving this requires separating intrinsic interfacial properties from the geometric and mechanical influences inherently embedded in microdroplet test results. The measured response is affected not only by the interface behavior but also by droplet geometry, blade position, fiber cross-section, matrix behavior, and many more (Dsouza et al., 2023). Consequently, the experimentally observed force–displacement response reflects the interaction of multiple parameters rather than a direct measure of interfacial behavior.

To isolate the interfacial response, a comprehensive numerical microdroplet model is required that accounts for the geometric complexity of natural fibers and the relevant material nonlinearities. In this work, a nonlinear finite element (FE) model is developed that incorporates non-circular fiber cross-sections, anisotropic fiber properties, potential interface anisotropy, and nonlinear matrix behavior. To the authors' knowledge, such a comprehensive model for microdroplet testing of natural fibers has not yet been reported.

The second main goal of the paper is to systematically analyze the sensitivity of the interface behavior, based on the established FE model. We aim to quantify the importance of individual input parameters and discuss their mutual dependencies. Given the interacting geometric and mechanical parameters, conventional one-factor-at-a-time sensitivity studies are insufficient because they neglect parameter interactions and nonlinear coupling. In practice, the influence of a single parameter often depends strongly on the values of others, making systematic exploration of the multidimensional parameter space computationally demanding when relying solely on finite element simulations.

This is the motivation to employ artificial neural networks (ANNs) as surrogate models trained on a large set of nonlinear finite element simulations. Once trained, ANNs provide a computationally efficient tool that enables global sensitivity analyses. Moreover, because the network consists of differentiable algebraic operations, derivatives of the force–displacement response with respect to input parameters can be computed efficiently, enabling a systematic evaluation of parameter influence and interaction.

These surrogates also pave the way for an efficient upscaling routine from microdroplet test to mesoscale biocomposite prediction, and thus to the biocomposite failure behavior. This is particularly important given that microdroplet tests for natural fibers typically yield large, highly scattered datasets, even for nominally identical specimens. In addition, experiments are often conducted across multiple material variants, including different polymers, fiber types, and fiber surface treatments, while environmental factors such as moisture and temperature further influence the results. Translating these numerous experimental datasets into consistent interfacial parameters for mesoscale composite models would require a large number of nonlinear simulations. The ANN surrogate therefore provides a fast and reliable alternative, enabling efficient interpretation of microdroplet tests and their translation into mesoscale biocomposite models.

To achieve the two main goals, the remainder of the paper is structured as follows: Section 2 starts with a detailed review of existing FE studies on microbond tests, highlighting their methodologies and key findings. This knowledge is then exploited to develop a novel FE model of microdroplet failure and to adopt and train an ANN model. Section 3 presents the results of the microdroplet simulations and the sensitivities regarding changes in geometrical and mechanical parameters. Section 4 finally concludes with key insights and directions for future research.

2. Microdroplet test simulations and neural network surrogate model

2.1. Overview of microdroplet FE simulations in the literature

This section provides an overview of the FE studies on microbond tests, summarized in Table 1. The table highlights the studied materials, assumptions for the FE models, adopted constitutive laws, and the objectives and key findings of each study. Organized chronologically by publication year, this breakdown underscores the advances in modeling interfacial mechanics and the evolving understanding of these systems.

The majority of studies rely on 2D axisymmetric models (2D_{ax}) (Schüller et al., 1998; Ash et al., 2003; Kang et al., 2009; Pandey et al., 2012; Li et al., 2017; Sato et al., 2017; Zhi et al., 2017; Nian et al., 2018; Bellil et al., 2023) for computational efficiency, although several have adopted 3D quarter models (3D_{qu}) (Pandey et al., 2012; Minnicino and Santare, 2012; Sockalingam et al., 2014) or full 3D models (3D) (Zhao et al., 2018; Dsouza et al., 2020, 2023) to better capture complex stress states. The droplet geometry is typically simplified as elliptical in profile (while circular in cross-section) (Schüller et al., 1998; Ash et al., 2003; Kang et al., 2009; Minnicino and Santare, 2012; Sockalingam et al., 2014; Li et al., 2017; Sato et al., 2017; Nian et al., 2018), but Carroll's fit (Carroll, 1976) is also commonly used to account for the meniscus formed by surface tension (Ash et al., 2003; Kang et al., 2009; Pandey et al., 2012; Zhao et al., 2018). Blades are often modeled as rigid, frictionless bodies (Ash et al., 2003; Kang et al., 2009; Pandey et al., 2012; Minnicino and Santare, 2012; Sockalingam et al., 2014; Li et al., 2017; Zhao et al., 2018), with parallel blade configurations only considered in 3D models (Pandey et al., 2012; Zhao et al., 2018; Dsouza et al., 2020, 2023). Most studies model flat vise angles ($\beta = 0^\circ$) (Ash et al., 2003; Pandey et al., 2012; Minnicino and Santare, 2012; Sockalingam et al., 2014; Li et al., 2017; Sato et al., 2017; Nian et al., 2018; Zhao et al., 2018) and sharp blade corners (Kang et al., 2009; Minnicino and Santare, 2012; Sockalingam et al., 2014; Li et al., 2017; Nian et al., 2018; Zhao et al., 2018; Dsouza et al., 2020, 2023). In some cases, the blades are not explicitly modeled, with boundary conditions applied directly to surface nodes of the droplet (Schüller et al., 1998; Zhi et al., 2017; Bellil et al., 2023). Isotropic (Iso.) linear elastic (LE) material models are frequently used for fibers and droplets (Schüller et al., 1998; Kang et al., 2009; Minnicino and Santare, 2012; Sockalingam et al., 2014; Li et al., 2017; Zhi et al., 2017; Nian et al., 2018; Bellil et al., 2023), although some studies incorporate plasticity for the droplet (Ash et al., 2003; Pandey et al., 2012; Sato et al., 2017; Dsouza et al., 2020, 2023) or thermal effects from droplet curing (denoted as α_T in Table 1) (Sockalingam et al., 2014; Sato et al., 2017; Zhao et al., 2018; Dsouza et al., 2023). For interface modeling, cohesive zone models (CZM) with bilinear traction–separation laws are widely employed and implemented exclusively via cohesive surfaces (Minnicino and Santare, 2012; Sockalingam et al., 2014; Li et al., 2017; Sato et al., 2017; Nian et al., 2018; Zhao et al., 2018; Dsouza et al., 2020, 2023). In some cases, the traction–separation laws are combined with Coulomb friction (μ) (Minnicino and Santare, 2012; Sockalingam et al., 2014; Zhao et al., 2018). However, mixed-mode behavior is not always included in these models.

This overview shows that capturing microdroplet behavior requires detailed modeling of geometry, interface properties, and boundary conditions. While many studies rely on simplifying assumptions – particularly regarding droplet shape and material behavior – we develop a 3D model that reflects the complexities of natural fiber composites, as described next.

Table 1

Overview of FEA approaches in microbond tests, summarizing materials, modeled geometry, constitutive behaviors, study objectives, and key findings. (continued on next page).

Materials	FEA Geometry			Material laws			Aim of the study	Findings/Comments	Ref.	
	Dim.	Droplet	Blade	Blade	Fiber	Droplet				Interface
glass / epoxy	2D _{ax}	elliptical	axisym. nodal constraints on droplet	–	Iso., LE	Iso., LE	fracture mechanics approach + μ	Investigate the influence of interfacial friction, geometry, and crack extension criteria using FEA and fracture mechanics.	Demonstrates how friction stabilizes crack extension. Highlights challenges of mixed-mode loading and elliptical geometry.	Schüller et al. (1998)
glass / polyester, glass / epoxy	2D _{ax}	elliptical, circular arc, Carroll's fit	axisym., round edge, $\beta = 0, 7, 14^\circ$	rigid, frictionless	Iso., LE	elastic-perfectly plastic	Interphase region, elastic-perfectly plastic	Study effects of bead geometry, interphase properties, and vise angle on stress distribution.	Significant impact of bead geometry (meniscus) and vise angle.	Ash et al. (2003)
carbon / epoxy	2D _{ax}	elliptical, cylindrical, Carroll's fit	axissym., sharp edge, $\beta \sim 20^\circ$	rigid, frictionless	Iso., LE	Iso., LE	not explicitly modeled (stresses at interface evaluated)	Evaluate (real) interfacial shear strength using FEA and experiments.	Suggests compensation factor (0.90–1.25) for stress concentrations for IFSS.	Kang et al. (2009)
carbon / epoxy	2D _{ax} , 3D _{qu}	Carroll's fit	parallel, round edge, $\beta = 0^\circ$	rigid, frictionless	Iso., LE	LE and elastic-perfectly plastic	not explicitly modeled (stresses at interface evaluated)	Evaluate effects of blade geometry and blade separation on stress distribution, failure modes and scatter.	3D model captures stress states better, highlighting limitations of shear-lag model.	Pandey et al. (2012)
glass / epoxy	3D _{qu}	elliptical	axisym., sharp edge, $\beta = 0^\circ$	rigid, frictionless	Iso., LE	Iso., LE	CZM with bilinear traction separation law (no mixed mode), + μ	Model the progressive damage of fiber–matrix interface using CZM. Study impact of geometry and material properties.	Mode II dominant, smaller microvise opening results in smaller zone of mixed mode interface.	Minnicino and Santare (2012)
glass / epoxy	3D _{qu}	elliptical	axisym., sharp edge, $\beta = 0^\circ$	rigid, frictionless	Iso., LE + α_T	Iso., LE + α_T	CZM with bilinear traction separation law (mixed mode: stresses and fracture toughness), + μ	Develop a detailed FE model including residual thermal stresses, friction and mixed mode to determine traction separation laws.	Highlights the impact of thermal pre-loading (curing) and droplet size on progressive failure. Identifies predominantly Mode II behavior, but mixed-mode initiation.	Sockalingam et al. (2014)
CNT / PMMA, CNT / PAA	2D _{ax}	elliptical	axisym., sharp edge, $\beta = 0^\circ$	rigid, frictionless	Iso., LE	Iso., LE	CZM with bilinear traction separation law (no mixed mode)	Investigate interfacial damage and failure mechanisms in CNT fiber/polymer composites to predict F - δ behavior.	Highlights complex stress distributions and non-linear interface behavior.	Li et al. (2017)

(continued on next page)

Table 1 (continued).

Materials	FEA Geometry			Material laws				Aim of the study	Findings/Comments	Ref.
	Dim.	Droplet	Blade	Blade	Fiber	Droplet	Interface			
carbon / TriA-X polyimide	2D _{ax}	elliptical	axisym., rounded edge, $\beta = 0^\circ$	high stiff., friction-less	Trans. Iso., LE + α_T	viscoelastic, plastic + α_T + dmg.	CZM with bilinear traction separation law (no mixed mode)	Accurately evaluate interfacial strength by combining experiments and FEA, incorporating thermo-viscoelasticity and resin damage.	Uses thermo-viscoelastic modeling to account for residual stresses. Highlights how resin damage initiates before interface failure.	Sato et al. (2017)
polyester fiber / epoxy	2D _{ax}	real geometry from exp.	axisym. nodal constraints on droplet	–	Iso., LE	Iso., LE	Coulomb friction (μ) model	Investigate effects of geometrical parameters (fiber diameter, embedded length, blade separation) on IFSS through experiments and FEA.	Identifies significant dependency of IFSS on fiber diameter, embedded length, and blade separation.	Zhi et al. (2017)
glass / epoxy	2D _{ax}	elliptical	axisym., sharp edge, $\beta = 0^\circ$	rigid, + μ	Iso., LE	Iso., LE	CZM that extends a bilinear traction separation law to account for post-peak friction (no mixed mode)	Propose and validate a CZM accounting for friction. Investigate the effects of geometrical and interfacial parameters on the IFSS through FEA and experiments.	Dimensional analysis links IFSS to a characteristic length scale, emphasizing the geometry's impact.	Nian et al. (2018)
carbon / epoxy	3D	Carroll's fit	parallel, sharp edge, $\beta = 0^\circ$	rigid, frictionless	Trans. Iso., LE + α_T	Iso., LE + α_T	CZM with bilinear traction separation law (mixed mode: stresses and fracture toughness), + μ	Study the effects of geometric and interfacial parameters (e.g., meniscus, blade geometry, and misalignment) on IFSS variability and failure mode;	Prismatic blades produce higher axial fiber stress than circular blades; Meniscus presence influences local stress distribution.	Zhao et al. (2018)
glass / epoxy	3D	real geometry from exp.	test setup fully modeled (parallel)	Iso., LE, frictionless	Iso., LE	elastic-plastic with kinematic hardening	CZM with bilinear traction separation law (mixed mode: fracture toughness)	Investigate interfacial debonding in microbond tests using local strain monitoring; validate 3D FE models for interfacial damage progression and fracture.	Highlights stages of fracture (elastic loading, crack nucleation, growth, and final debonding). Local strain monitoring improves accuracy of F- ϵ relationships.	Dsouza et al. (2020)
glass / epoxy	3D	as above	as above	as above	Iso., LE + α_T	LE, elastic-plastic with perfect, isotropic, kinematic hardening	as above	Investigate the interdependencies between droplet geometry, thermal residual stresses, material properties, and interfacial behavior in microdroplet tests using experiments and FEA.	Explores how geometric variations, material hardening, and curing-induced residual stresses mutually influence interfacial debonding.	Dsouza et al. (2023)
flax / thermo-plastics (PLA, PBS, PP, MAPP, PHA)	2D _{ax}	elliptical	axisym. nodal constraints on droplet	–	Iso., LE	Iso., LE	spring like zero thickness layer similar to CZM, linear + exponential debonding	Predict the interfacial stiffness, critical separation, and debonding propagation in flax fiber-reinforced thermoplastics by experiments and FEA.	Explores interfacial parameters of a simplified traction separation law.	Bellil et al. (2023)

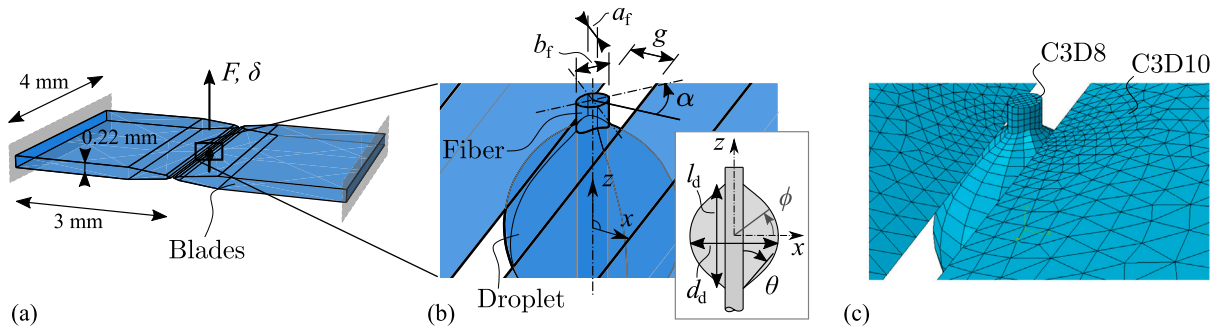


Fig. 1. Overview of the finite element (FE) analysis setup for microdroplet tests. (a) Full simulation model displaying the blades and their fixation (in gray), (b) a close-up view of the fiber-droplet configuration between the blades and its geometric definitions, and (c) discretization of the model and selected element types for the fiber, droplet, and blades.

2.2. FE model

2.2.1. Geometry

Given our interest in systematically studying the effects of changes in geometry and interfacial behavior on the stress–strain response measured in microdroplet tests of biocomposites, we aim for a fully parametrizable 3D model. Geometrical parameters of the fiber-droplet-blade test frame, see Fig. 1, are discussed first. To account for the natural shape variability characteristic of plant fibers, the fiber is modeled with an elliptical cross-section defined by a minor axis length a_f and major axis length b_f . This deviation from a circular geometry introduces the fiber's rotational orientation α relative to the blades [Fig. 1(b)] as an additional parameter—making this the first model to explicitly incorporate fiber rotation. While such non-circular cross-sections are particularly pronounced in natural fibers, comparable deviations from ideal circularity have also been reported for synthetic fibers (Thomason et al., 2024). The fiber is truncated just above the droplet, unlike experimental configurations with long free fiber segments that contribute to the total displacement (Hampe and Marotzke, 1997; Minnicino and Santare, 2012; Sockalingam et al., 2014). As this contribution depends linearly on the (often undocumented) free fiber length and can be described analytically by linear elasticity, it is omitted here to isolate the response of the droplet-interface system. The truncated end is pulled in the z -direction, with load and displacement tracked at this position. The fiber extends below the droplet by a length equal to the droplet itself, ensuring consistent fiber-droplet contact throughout the simulations.

The droplet itself is modeled with a circular cross-section, sharing a common center with the elliptical fiber. To approximate the droplet's shape in the longitudinal direction, Carroll's method (Carroll, 1976; Song et al., 1998; Ash et al., 2003) is adopted, accounting for the meniscus with contact angle θ formed by surface tension when applying the polymer to the fiber. Thus, the parametric profile of the quarter of the droplet that is located in the positive xz -plane as a function of the elevation ϕ (angle from x) reads as

$$x = \frac{1}{2} l_d \sqrt{1 - k^2 \sin^2(\phi)}, \quad \forall 0 \leq \phi \leq \phi_{\max} \quad (1)$$

$$z = \frac{1}{2} [m a_f E_1(\phi, k) + l_d E_2(\phi, k)],$$

with

$$m = \frac{l_d \cos(\theta) - a_f}{l_d - a_f \cos(\theta)}, \quad (2)$$

$$k = \sqrt{\frac{l_d^2 - (m a_f)^2}{l_d^2}}, \quad (3)$$

and where $E_1(\phi, k)$ and $E_2(\phi, k)$ are the incomplete elliptic integrals of the first and second kinds, respectively, and where ϕ_{\max} marks the

angle at which the bead meets the fiber surface:

$$\phi_{\max} = \arcsin \left(\frac{1}{k} \sqrt{1 - \frac{a_f^2}{l_d^2}} \right). \quad (4)$$

The profile is then mirrored around the x -axis and revolved around the z -axis to generate a 3D droplet shape, which is subsequently intersected with the elliptical fiber geometry. Finally, the razor blades are used in the test setup and modeled sufficiently large to align with typical test configurations and to capture deformations resulting from potential bending. The blades are positioned parallel to each other, similar to setups described in the literature (Zhi et al., 2017; Nian et al., 2018; Bellil et al., 2023). Each blade has a two-sided double bevel at a 20° angle, and a thickness of 0.22 mm. In the model, the blade width extends to 3 mm up to the fixation point, with a length of 4 mm, as shown in Fig. 1(a). The blade distance g can significantly affect the stress distribution and resulting apparent IFSS (Chou et al., 1994; Pisanova et al., 2001; Ash et al., 2003; Kang et al., 2009). The minimum blade distance g_{\min} is determined by the geometric constraints that the blades do not intersect the fiber

$$g_{\min} = a_f \sqrt{\left(\frac{b_f \cos(\alpha)}{a_f} \right)^2 + \sin^2(\alpha)}, \quad (5)$$

while the maximum blade distance is set equal to the droplet diameter, $g_{\max} = d_d$. In between these bounds, we define the blade distance by a normalized input n_g , with $0 \leq n_g \leq 1$ as

$$g = g_{\min} + n_g \cdot (g_{\max} - g_{\min}), \quad (6)$$

where $n_g = 0$ corresponds to blades touching the fiber ($g = g_{\min}$), and $n_g = 1$ corresponds to blades only touching the outer perimeter of the droplet ($g = g_{\max}$).

2.2.2. Constitutive material behavior

A flax-MAPP (Maleic Anhydride-grafted Polypropylene) biocomposite was selected as the basis of our study due to the availability of extensive experimental data for interface, fiber, matrix, and composite (Bourmaud et al., 2013; Pantaloni et al., 2021; Bellil et al., 2023). In this study, the matrix droplet and fiber bulk properties are kept constant throughout, to focus solely on variations of interfacial mechanical properties. The matrix material is modeled using von Mises plasticity with isotropic hardening. This choice reflects the ductile behavior observed in experimental stress–strain curves of the pure polymer material, which show gradual yielding and hardening rather than abrupt failure. Specifically, the yield stress and the isotropic hardening parameters were directly calibrated using the experimental stress–strain data of the pure MAPP matrix as reported by Pantaloni et al. (2021). Linear elasticity is assumed up to 25% of the peak stress, with the Young's modulus likewise derived from these experimental benchmarks, see Fig. 2 or Table 2 for further details.

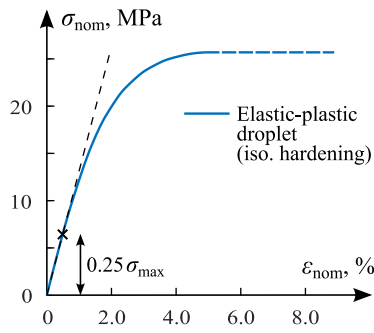


Fig. 2. Nominal stress–strain response of the MAPP matrix.
Source: Extracted and adapted from Pantaloni et al. (2021).

Table 2
Fixed Mechanical parameters used for the microbond simulations.

Blades (Steel)		Fiber (flax) ^a		Matrix (MAPP) ^b	
E	210 GPa	C_{llll}	51.6 GPa	E	1580 MPa
ν	0.30	C_{rrrr}	7.14 GPa	ν	0.43
		C_{llrr}	2.63 GPa	σ_y	6.46 MPa
		C_{rrtt}	2.58 GPa	\vdots	\vdots
		C_{lrrr}	2.28 GPa	$\sigma_n, \epsilon_n^{pl}$	27.00, 0.03972

^a As in Senk et al. (2025).

^b For a complete list of parameters, see Senk et al. (2025).

The fiber properties are based on single-fiber tensile tests from the same experimental dataset (Bourmaud et al., 2013). To account for the anisotropic characteristics of plant fibers, the elastic stiffness tensor is determined using a multiscale micromechanics model (Königsberger et al., 2023), assuming transversely isotropic behavior. An overview of the constant mechanical properties used in the model is provided in Table 2.

The fiber-droplet interface is represented by a bilinear traction–separation law using cohesive surfaces. The traction t_i ($i \in \{n, s, t\}$, with normal (n), shear (s), and tangential (t) direction) is related to separations δ_i through an uncoupled stiffness tensor:

$$\begin{bmatrix} t_n \\ t_s \\ t_t \end{bmatrix} = \begin{bmatrix} K_{nn} & 0 & 0 \\ & K_{ss} & 0 \\ \text{sym.} & & K_{tt} \end{bmatrix} \cdot \begin{bmatrix} \delta_n \\ \delta_s \\ \delta_t \end{bmatrix}, \quad (7)$$

where K_{ii} are the stiffness components. Interfacial damage initiates when a maximum stress criterion is met:

$$f_{\text{init}} = \max \left\{ \frac{t_n}{t_{n,\text{ult}}}, \frac{|t_s|}{t_{s,\text{ult}}}, \frac{|t_t|}{t_{t,\text{ult}}} \right\} \geq 1, \quad (8)$$

with $t_{i,\text{ult}}$ as direction-dependent interface strength. Damage evolution is governed by a mixed-mode criterion to assess the relevance of energy contributions in directions other than the shear direction, reading as

$$\frac{G_n}{G_{n,c}} + \frac{G_s}{G_{s,c}} + \frac{G_t}{G_{t,c}} = 1, \quad (9)$$

incorporating direction-specific fracture energies G_i and critical fracture energies $G_{i,c}$.

The interfacial parameters, including strengths $t_{i,\text{ult}}$ and fracture energies $G_{i,c}$, are treated as variable inputs in this study and are systematically analyzed in the results in Section 3.2.3. Among these, the directions s and t correspond to Mode II and Mode III fracture behavior, respectively. While the actual stress or separation states may differ in these directions, we assume equal interface strengths ($t_{s,\text{ult}} = t_{t,\text{ult}}$) and critical fracture energies ($G_{s,c} = G_{t,c}$) in all simulations. For simplicity, only the subscript s is used to refer to shear-related parameters in the remainder of the text and figures. The stiffness components of the uncoupled traction–separation law are kept constant throughout all

analyses, using high, yet numerically stable values, as discussed in Senk et al. (2025).

Coulomb friction is considered a variable input between the fiber and droplet, as well as between the droplet and the blades, as friction is essential for accurately capturing interfacial mechanics, especially for capturing post-peak behavior (Nian et al., 2018). This way, two friction coefficients are defined: the blade-to-droplet friction coefficient μ_{blade} , and the fiber-to-droplet interface friction coefficient μ_{intf} .

2.2.3. Numerical aspects

The mesh consists of ten-node tetrahedral elements with a quadratic shape function (C3D10) for the blades. The fiber-droplet system employs eight-node linear hexahedral elements with a linear shape function (C3D8), with approximately 1600–2000 elements, as shown in Fig. 1(c) and discussed in more context in a mesh study in Section 3.1.

Implicit geometric nonlinear static analysis is performed in Abaqus (Abaqus, 2024). Viscous regularization is applied to ensure numerical stability. While artificial viscosity stabilizes the solution, excessive stabilization can distort results, necessitating careful monitoring of its impact. Following the approach outlined in prior work (Senk et al., 2025; Vida et al., 2022, 2023), we adopt an energy-based criterion to evaluate the influence of stabilization energies:

$$f_{\text{cri}} = \frac{E_{\text{ALLCD}}}{E_{\text{ALLIE}}} \leq 0.1\%, \quad (10)$$

where E_{ALLIE} is the total strain energy in the system, and E_{ALLCD} represents energy related to viscous regularization of interfacial failure, set with a viscosity coefficient of $1 \cdot 10^{-5}$. The energy criterion (10) is evaluated in a postprocessing step to confirm that the stabilization energy E_{ALLCD} consistently remains within a strict threshold of 0.1%.

2.3. Neural network approach

2.3.1. Sampling strategy

To enable the systematic study of parameter effects on the micro-droplet test behavior, the Abaqus model was fully parameterized for both geometrical and interfacial parameters. Seven variable geometrical parameters (see Fig. 1(b)) are considered in this study, including three related to the droplet, three related to the fiber, and one associated with the test rig. The droplet geometry is described by its diameter d_d , its length-to-diameter ratio l_d/d_d , and the contact angle between fiber and droplet θ . The fiber geometry is quantified by the diameter along the minor axis of the elliptical cross section, a_f , the aspect ratio b_f/a_f of this cross section, and the fiber rotation angle α . Finally, the test setup is characterized by the normalized blade distance n_g . Six variable interfacial (mechanical) parameters are considered, including the mode I fracture energy G_n and mode II/III fracture energies G_s , along with the interface strengths in mode I, t_n , and mode II/III, t_s . Additionally, the two friction coefficients μ_{blade} and μ_{intf} are varied.

To efficiently sample the parameter space while ensuring good coverage of all parameter combinations, a Latin Hypercube Sampling (LHS) approach is used. LHS ensures that each parameter is sampled evenly across its range while maintaining a near-random distribution, making it particularly suitable for high-dimensional parameter spaces (McKay et al., 1979; Iman and Conover, 1980). For this study, the Julia package LatinHypercubeSampling.jl (Urquhart et al., 2020) was employed.

Each model was simulated using Abaqus on a high-performance computing cluster. For the chosen discretization (detailed in the mesh sensitivity study in Section 3.1), individual simulations require approximately 2–3 h of wall-clock time. To optimize throughput, simulations are executed in parallel using 4 threads per run on a compute node equipped with two 24-core AMD EPYC 7402 CPUs (totaling 96 threads) and 512 GB of RAM. Simulations that failed due to convergence issues or problematic parameter combinations were automatically excluded. Only those that captured the full load–displacement behavior – including the peak load and full degradation (either to zero force or a plateau

in cases where interfacial friction was considered) – were retained for further analysis. A small number of simulations exhibiting clearly unrealistic responses (e.g., excessive displacements or non-physical force–displacement curves) were manually filtered out and affected only a few isolated edge cases in which individual elements experienced extreme distortions.

The primary output of each simulation is the force–displacement (F – δ) curve obtained under displacement-controlled loading. Rather than directly analyzing these curves, we normalize the force by the embedded area A_{emb} to obtain the apparent shear stress $\tau_{\text{app}} = F/A_{\text{emb}}$, enabling comparison across different geometrical configurations.

To prepare the stress–displacement curves for training a neural network, the raw τ_{app} – δ data were first smoothed and then resampled. This preprocessing step is necessary because the ANN requires input data with a fixed resolution and predefined δ limits. In contrast, the adaptive load incrementation scheme used in Abaqus produces δ values that are unevenly spaced and vary between configurations. To smooth the τ_{app} – δ curves while preserving key features such as the peak load, a Savitzky-Golay filter (Savitzky and Golay, 1964) with a window size of 3 and a polynomial order of 1 was applied. Following this, the filtered data were resampled to 150 uniformly spaced points using linear interpolation, ensuring that all simulations – regardless of their original output length – were represented by a consistent number of τ_{app} – δ pairs.

2.3.2. Neural network architecture and training

The neural network used in this study is a fully connected feedforward model implemented as a Multi-Layer Perceptron (MLP) using the Julia package Flux.jl (Innes, 2018; Innes et al., 2018). The architecture is specifically designed to capture the non-linear relationships between the input parameters and the output τ_{app} – δ curves. The ANN structure is as follows:

- An input layer with n neurons, matching the dimensionality of the current parameter space.
- Two hidden layers, each containing $4 \cdot n$ neurons and using the Rectified Linear Unit (RELU) as the activation function.
- A dropout rate of 40% is applied after each hidden layer to reduce overfitting for small datasets by randomly deactivating neurons during training.
- An output layer consisting of $N = 150$ neurons, representing the predicted apparent shear stress $\hat{\tau}_{\text{app}}$ for a predefined range of δ values (see Fig. 3).

All variable (geometrical or mechanical) input parameters were min–max normalized to the space $\mathbf{I} = [0, 1]$. Define $\mathbf{x}_i \in \mathbf{I}^n$ as the i th realization of the parameter space. The model's prediction performance is evaluated using the mean absolute error (MAE) between the predicted and target curves. The MAE loss for a single (i th) parameter configuration is defined as

$$\text{MAE}_i = \frac{1}{N} \sum_{j=1}^N \left| \tau_{\text{app},i,j} - \hat{\tau}_{\text{app},j}(\mathbf{x}_i) \right|, \quad (11)$$

where N is the number of output points, $\tau_{\text{app},i,j}$ is the ground truth value from the resampled FE simulations for configuration i at displacement δ_j , and $\hat{\tau}_{\text{app},j}(\mathbf{x}_i)$ is the corresponding ANN prediction. The total loss minimized during training is the mean absolute error \mathcal{L}_{MAE} over all training samples:

$$\mathcal{L}_{\text{MAE}} = \frac{1}{MN} \sum_{i=1}^M \sum_{j=1}^N \left| \tau_{\text{app},i,j} - \hat{\tau}_{\text{app},j}(\mathbf{x}_i) \right|, \quad (12)$$

where M is the number of training samples. The model is optimized using the Adam optimizer with a learning rate of 0.001, and it is trained for up to 10 000 epochs using a batch size of eight. The dataset is split into 80% for training and 20% for validation.

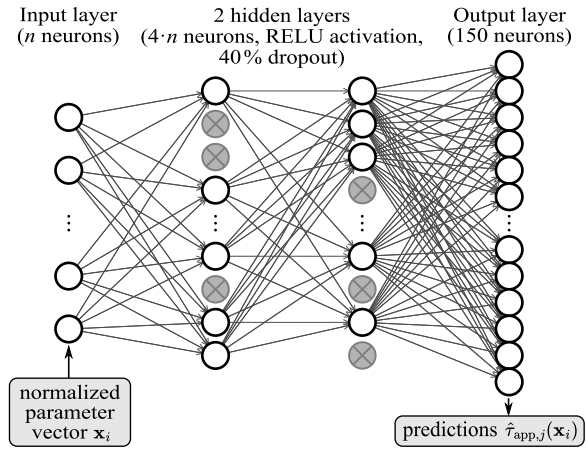


Fig. 3. Architecture of the ANN model. The network maps the normalized parameter vector \mathbf{x}_i to predicted shear stress curves $\hat{\tau}_{\text{app},j}(\mathbf{x}_i)$ at 150 uniformly spaced displacements δ_j via two hidden layers with RELU activation and 40% dropout.

2.3.3. Gradient-based sensitivity analyses

Beyond its predictive capability, the ANN offers the unique ability to compute derivatives of the $\hat{\tau}_{\text{app}}$ – δ response with respect to individual inputs x_i . ANNs are well-suited for this task as they are composed of a series of trivial algebraic function evaluations. Thus, automatic differentiation can be applied, enabling a systematic sensitivity analysis that allows the effects of each parameter to be studied independently—a task that would be rather difficult to achieve with traditional FE simulations alone due to the mutual dependencies among parameters (Dsouza et al., 2023).

Following the notation from Section 2.3.2, for each predicted value $\hat{\tau}_{\text{app},j}(\mathbf{x})$, where $\mathbf{x} \in \mathbf{I}^n$, the first-order sensitivity with respect to a single parameter x_i at δ_j can be quantified by

$$\frac{\partial \hat{\tau}_{\text{app},j}(\mathbf{x})}{\partial x_i}. \quad (13)$$

The value of the partial derivative in Eq. (13), which quantifies the local sensitivity of $\hat{\tau}_{\text{app},j}$ to x_i , can vary significantly depending on the specific point \mathbf{x} within the input space \mathbf{I}^n . This variation reflects the non-linear relationships and learned interdependencies among all input parameters as captured by the ANN. Thus, to fully quantify a sensitivity, Eq. (13) is evaluated for all $\mathbf{x} \in \bar{\mathbf{I}} \subset \mathbf{I}^n$, where $\bar{\mathbf{I}} = \{0, 0.1, \dots, 1\}$, leading to a range of sensitivity values, further described by their interquartile range and average.

Beyond individual partial derivatives, the Hessian matrix offers a viable measure for mutual and self-dependency. A second-order dependency between the parameters $x_i, x_k \in \mathbf{I}$, can be obtained by evaluating

$$\frac{\partial^2 \hat{\tau}_{\text{app},j}(\mathbf{x})}{\partial x_i \partial x_k} \quad \forall \mathbf{x} \in \bar{\mathbf{I}} \subset \mathbf{I}^n \text{ and } \forall j. \quad (14)$$

Entries on the diagonal ($i = k$) indicate how the sensitivity of a parameter is affected as the parameter itself varies, while off-diagonal terms ($i \neq k$) characterize the change in sensitivity when another parameter varies. As the procedure for computing the Hessian of large problems is computationally intensive, it should be limited to characteristic values of the $\hat{\tau}_{\text{app}}$ – δ curves, such as the maximum. This effectively reduces the number of possible values for j . In addition, by assessing the approximation error of a second-order Taylor series expansion utilizing both Eqs. (13) and (14), the density of the space $\bar{\mathbf{I}}^n$ can potentially be reduced.

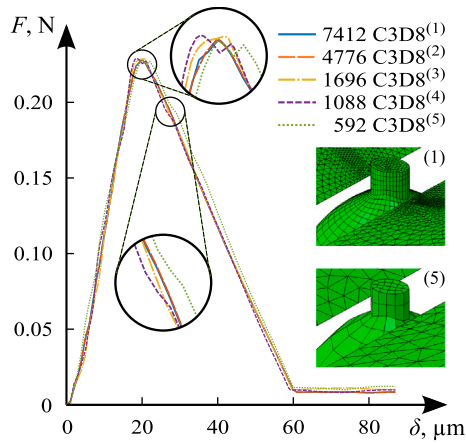


Fig. 4. FE-predicted force–displacement (F - δ) curves using different mesh configurations—from the finest (1) to the coarsest (5) discretization.

3. Results of the microdroplet simulations

3.1. Mesh study

First, a mesh sensitivity study was conducted to ensure the reliability of the FE simulations across different parameter configurations. The fiber-droplet configuration was discretized using hexahedral elements with a linear shape function (C3D8), with element counts ranging from 592 to 7412, as shown in Fig. 4. The mesh was refined near the droplet's contact region with the blades to capture localized stress distributions better.

The parameter set chosen for this study represents typical geometrical and mechanical characteristics based on the flax-MAPP configuration reported by Pantaloni et al. (2021). This set includes mean geometrical values ($d_d = 162 \mu\text{m}$, $l_d = 220 \mu\text{m}$, $a_f = 21 \mu\text{m}$, and $\theta = 25.7^\circ$), combined with a non-circular fiber cross-section ($b_f/a_f = 1.5$) and a rotated fiber orientation ($\alpha = 30^\circ$), introducing both complexity and realistic variability to the test case. The interfacial mechanical parameters were selected based on earlier mesoscale studies (Senk et al., 2025) and include $G_i = 0.30 \text{ Nmm/mm}^2$, $t_i = 12.74 \text{ N/mm}^2$ (where $i \in n, s$), and friction coefficients of $\mu_{\text{intf}} = 0.3$ and $\mu_{\text{blade}} = 0.3$.

The resulting force–displacement (F - δ) curves from the simulations show good agreement across all mesh configurations, indicating overall mesh independence. However, a detailed comparison (see magnified views in Fig. 4) reveals that the coarsest models (Cases 4 and 5) produce significant numerical noise and non-physical artifacts, such as “double peaks” at the maximum load. These features likely arise from localized element-level distortions and do not represent the physical debonding process. Such numerical noise is detrimental to ANN training, as it prevents the model from distinguishing between calculation errors and actual physical trends.

While the finest configurations, Case (1) and Case (2), provide the most stable and overlapping results, their significantly higher computational cost makes them impractical for the hundreds of simulations required for sampling. Consequently, a mesh density corresponding to approximately 1600–2000 elements for the fiber-droplet system (as in Case 3) is selected, maintaining computational efficiency required for large-scale dataset generation while ensuring a smooth enough response for ANN training. Furthermore, it accounts for other parameter configurations where numerical artifacts might be even more prevalent.

3.2. Sensitivity studies

In this section, the sensitivity of the microdroplet test results is systematically quantified with respect to variations in geometric and

mechanical parameters. To maintain a high sampling density and ensure the robustness of the surrogate model, the analysis is partitioned into three subsections.

This structure is motivated by the high-dimensional nature of the parameter space: varying all 7 geometrical and 6 mechanical variables simultaneously would require an prohibitively large training dataset to achieve accurate predictions. By separating the geometrical and mechanical sub-spaces, the required sample size remains computationally manageable while maintaining high predictive accuracy and simplifying the interpretation of the results.

The workflow begins with a preliminary study to determine the most appropriate fixed mechanical baseline, as different mechanical interfacial properties may alter the observed geometric sensitivity. This is followed by a surrogate-based geometrical sensitivity analysis, where the ANN is trained on a varied geometric dataset while holding mechanical properties constant. Finally, a mechanical sensitivity analysis is conducted, where the interfacial properties are varied against a fixed geometric configuration to isolate their specific influence on the debonding process.

3.2.1. Preliminary study on geometrical sensitivity

To study the role of geometry in isolation, the interfacial mechanical properties must be held constant. However, the sensitivity to geometric changes is strongly dependent on these fixed values, particularly in cases where mechanical properties are uncoupled or overly simplified. A preliminary study is therefore necessary to identify a representative mechanical parameter set that captures the relevant physical sensitivities of the test.

The ranges of the seven variable geometrical parameters ($n = 7$) are based on the microdroplet tests for the flax-PP biocomposite reported by Pantaloni et al. (2021) and are summarized in Table 3. In more detail, the droplet geometry – diameter (d_d), length-to-diameter ratio (l_d/d_d), and contact angle (θ) – was considered to vary within one standard deviation from the reported mean. The minor axis length of the fiber's elliptical cross-section a_f corresponds to the range of fiber diameters listed by Pantaloni et al. (2021). The fiber aspect ratio b_f/a_f , in turn, was set to vary up to 2.5, while the fiber rotation angle α ranges from 0° to 90° , representing all possible orientations. The normalized blade distance n_g ranges from 0.1 to 0.6. The lower limit of 0.1 avoids numerical issues caused by the blades being too close to the fiber. In contrast, the upper limit of 0.6 minimizes the droplet distortions before the stresses transfer to the interface.

The constant mechanical parameters, in turn, first remain consistent with those used in the mesh study, except that interfacial friction is set to zero, see the parameters listed for the benchmark case (a) in Table 3. Thereafter, two further sets of (constant) mechanical properties are used to study geometrical sensitivity effects. Interfaces tend to be weak upon debonding in normal direction (Mode I) due to lack of adhesion (Dzenis and Qian, 2001; Kim and Mai, 1991; Camanho and Davila, 2002). This is particularly pronounced in biocomposites, where natural fiber interfaces exhibit greater variability in adhesion quality, leading to more brittle behavior under normal loading conditions (Pantaloni et al., 2021). This way, in Case (b), the traction in the normal direction is significantly reduced to 50% of that being reported in literature (Pantaloni et al., 2021), resulting in $t_n = 4.90 \text{ MPa}$, while keeping the other tractions and fracture energies at their benchmark values (see Table 3). In Case (c), the fracture energy in the normal direction is substantially reduced to $G_n = 0.0015 \text{ Nmm/mm}^2$, while the other values remain unchanged. For each of the three cases of mechanical properties, 100 fiber-droplet configurations were generated and simulated with FE.

First, the resulting shear stress–displacement curves are analyzed. As for the benchmark case, the maximum shear stress $\tau_{\text{app,max}}$ remains close to the interfacial shear strength t_s of 12.74 MPa for all geometrical variations, see Fig. 5(a). The displacement at peak stress, however,

Table 3

Ranges of variable geometrical parameters and fixed mechanical parameters for three study cases.

Geometrical Parameters, compare Fig. 1(b).						
d_a^a (μm)	l_a/d_a^a (-)	a_f^a (μm)	θ^a ($^\circ$)	b/a_f (-)	α ($^\circ$)	n_g (-)
98–233	1.16–1.48	13–31	13.6–31.4	1.0–2.5	0–90	0.1–0.6
Mechanical Parameters from Senk et al. Senk et al. (2025)						
	t_n (MPa)	t_s (MPa)	G_n (Nmm/mm ²)	G_s (Nmm/mm ²)	μ_{blade} (-)	μ_{intf} (-)
Case (a)	12.74	12.74	0.30	0.30	0.6	0
Case (b)	4.90	12.74	0.30	0.30	0.6	0
Case (c)	12.74	12.74	0.0015	0.30	0.6	0

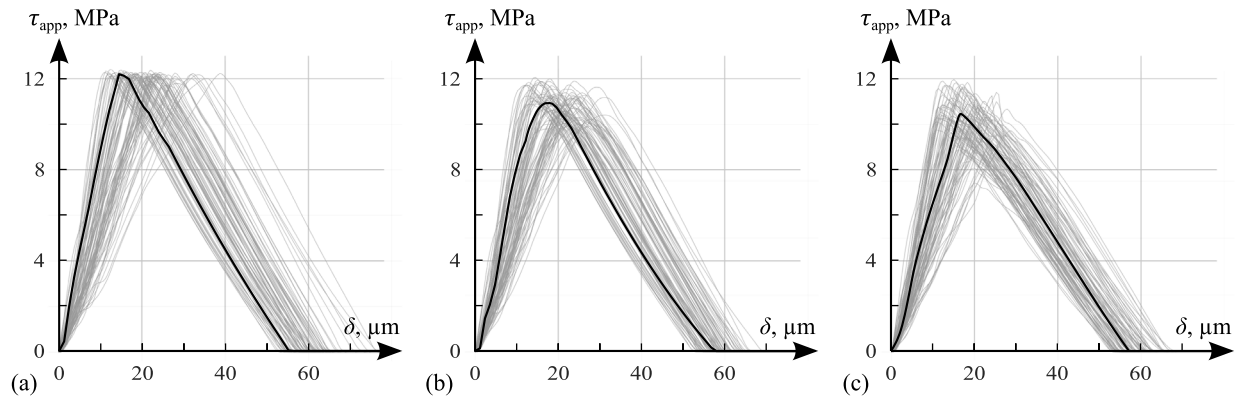
^a As reported by Pantaloni et al. (2021), Bellil et al. (2023).

Fig. 5. Apparent shear stress–displacement ($\tau_{\text{app}}-\delta$) curves showing the geometric sensitivity for three cases of mechanical properties: (a) Baseline properties, (b) reduced normal traction t_n , and (c) reduced normal fracture energy G_n ; individual FE simulations are given in (gray), the black curves highlight the simulations closest to the mean of $\tau_{\text{app,max}}$.

ranges from 10 to 40 microns. This demonstrates that if interface properties (strength and fracture energy) are independent of the direction, the microdroplet test is indeed suitable for quantifying the interfacial shear strength by dividing the applied force by the embedded area. This is no longer the case when failure properties in normal directions are reduced, see Cases (b) and (c). Then, mixed-mode interactions lead to generally smaller peak stresses (see the representative black line closest to the median of $\tau_{\text{app,max}}$ in Fig. 5(b)–(c)) and geometrical variations lead to significant changes not only in displacements at peak stress but also in the peak stresses themselves.

3.2.2. Surrogate-based geometrical sensitivity analysis

To further investigate the sensitivity of the individual geometrical parameters, Case (c) was selected as the basis for ANN training. In this context, each of the seven variable geometrical parameters is referred to as x_i , forming the components of the normalized input vector $\mathbf{x} \in \mathbb{I}^7$. The choice of Case (c) over Case (b) is motivated by its slightly stronger response to mixed-mode interactions, making it a suitable dataset for learning the influence of geometrical variations on interfacial failure. To ensure a sufficiently large and diverse dataset, the initial 100 FEA simulations were extended to 300 samples. After filtering, 13 samples were excluded due to either automatic (e.g., convergence issues) or manual (e.g., non-physical behavior) criteria. The remaining 287 configurations were split into 230 training samples and 57 validation samples. To evaluate the robustness of the ANN approach, training and validation datasets were shuffled in repeated training runs, verifying consistent results across splits. While the dataset is compact, the use of dropout layers prevents overfitting, and the high fidelity of the used mesh ensures that the model learns from clean physical signals rather than numerical artifacts.

Both training and validation loss converge rather quickly to values amounting to mean average errors \mathcal{L}_{MAE} of 0.17 MPa and 0.20 MPa, respectively, see Fig. 6. Fig. 7 demonstrates the ANN’s ability to replicate the “truth” of the FEA simulations for the unseen validation

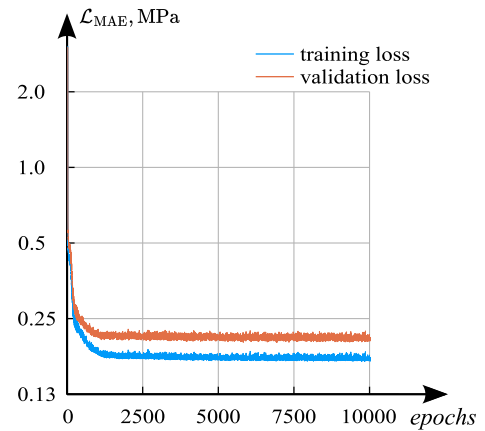


Fig. 6. Training and validation loss over 10 000 epochs.

dataset very accurately. The best prediction (Fig. 7(a)) aligns almost perfectly with the ground truth, the median prediction only exhibits minor discrepancies (Fig. 7(b)) and even the worst prediction (Fig. 7(c)) remains sufficiently accurate. Notably, the ANN training process was designed to avoid overfitting by incorporating dropout layers. Therefore, an additional smoothing of the data is expected.

The trained and validated neural network is finally utilized to study the sensitivity of the results with respect to changes in the geometric input parameters. Fig. 8 presents the results of this study. To illustrate the impact of geometrical variations in Fig. 8(a), the ANN is first used to show the mean and representative quantiles (5, 25, 75, and 95%) of the apparent shear stress as functions of the displacement. The corresponding quantile bands (5–95% quantile band in light gray, 25–75% quantile band in dark gray) underline that geometric variability manifests in

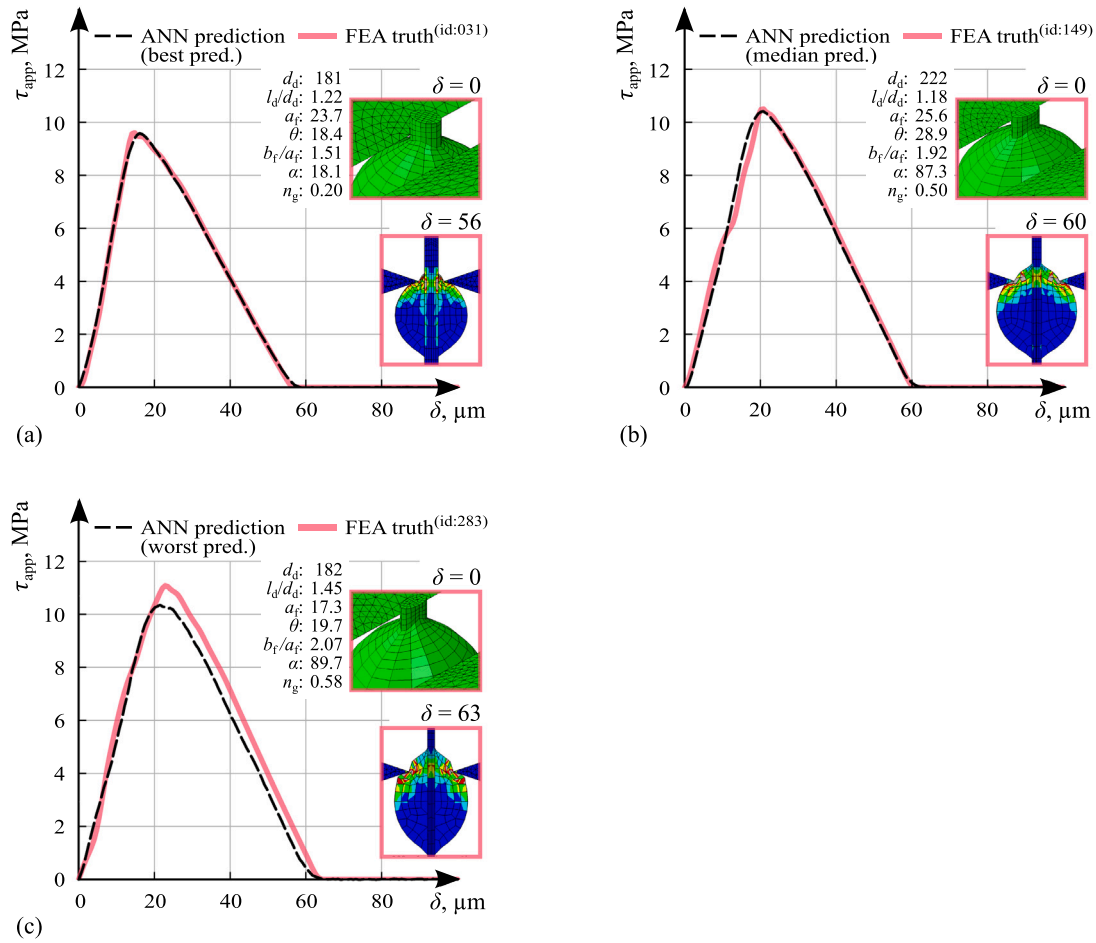


Fig. 7. Comparison of ANN predictions (black dashed lines) with smoothed and resampled FEA simulation results (light red lines) for (a) the best, (b) median, and (c) worst predictions within the validation dataset. Each subplot also includes a 3D view of the meshed initial fiber-droplet configuration with all corresponding geometrical parameters and a vertical 2D cross-section through the fiber axis of the deformed state with von Mises stress overlay.

substantial differences across the whole stress–displacement curves. Notably, peak stresses and corresponding displacements at peak stress vary significantly, as already seen in Fig. 7(c).

The actual benefit of training the ANN lies in the possibility of analyzing the effects of each individual input based on gradients, as explained in the Methods (Section 2.3.3). Fig. 8(b) displays the ANN-based stress gradients with respect to the individual input parameters as a function of the displacement. For every displacement point δ_j , the partial derivative $\partial \hat{\tau}_{app,j} / \partial x_i$ is computed across a grid of input parameter vectors $\mathbf{x} \in \mathbb{I}^n$. This yields a range of gradient values for each x_i and δ_j , from which the mean (solid line) and interquartile range (shaded area) are shown.

In Fig. 8(b), the magnitude of the gradients reflects the degree of sensitivity, with higher absolute values (positive or negative) indicating a stronger influence of the parameter on the output curve. Notably, a wide interquartile range in the gradient distributions highlights that sensitivity varies considerably across configurations, pointing to complex interactions and potential nonlinear effects within the parameter space. Positive gradients $\frac{\partial \hat{\tau}_{app,j}}{\partial x_i} > 0$ indicate that increasing a parameter x_i leads to a higher shear stress $\hat{\tau}_{app,j}$ at displacement δ_j , while negative gradients $\frac{\partial \hat{\tau}_{app,j}}{\partial x_i} < 0$ imply that increasing x_i reduces the measured stress response.

The fiber diameter (a_f) exhibits the strongest influence on the predicted $\hat{\tau}_{app}$, particularly near the peak stress. An increase in a_f leads to a pronounced decrease in $\hat{\tau}_{app}$ in this region, thereby reducing the maximum apparent shear stress $\hat{\tau}_{app,max}$. This behavior is consistent

with findings by Zhi et al. (2017), who reported higher IFSS for smaller fiber diameters. The effect likely stems from a combination of stress distribution characteristics and the embedded area normalization: although the force is normalized by the fiber–matrix interface area, the reduction in τ_{app} with increasing diameter remains significant. In the post-peak region, a slight shift toward positive gradients suggests that larger fiber diameters may delay stress decay, possibly due to a more distributed energy release or a broader cohesive zone.

Similarly, the aspect ratio b_f/a_f , which also involves a_f , shows a comparable influence pattern: in the peak regime, increasing the aspect ratio – i.e., making the fiber more non-circular – reduces apparent shear stress $\hat{\tau}_{app}$. The droplet dimensions, namely the droplet diameter (d_d) and length-to-diameter ratio l_d/d_d , exhibit similar but less pronounced effects compared to the fiber diameter. In the pre-peak and peak regimes, increasing either parameter leads to a lower apparent shear stress $\hat{\tau}_{app}$. This suggests that larger or more elongated droplets alter the stress distribution along the interface in a way that reduces the measured macroscopic stress response. In the post-peak regime, the slight positive gradients imply that these geometrical changes may contribute to a more gradual decrease of $\hat{\tau}_{app}$ after failure. In contrast, the fiber rotation angle (α) shows minimal influence across all regimes. The contact angle (θ), within the narrow range considered, similarly has a negligible impact on $\hat{\tau}_{app}$. However, its influence might become more pronounced if the droplet geometry were modeled elliptically rather than using Carroll’s method, as suggested by several studies (Ash et al., 2003; Kang et al., 2009). Interestingly, the blade distance (n_g) exhibits the most positive influence on $\hat{\tau}_{app}$ after the peak. This is

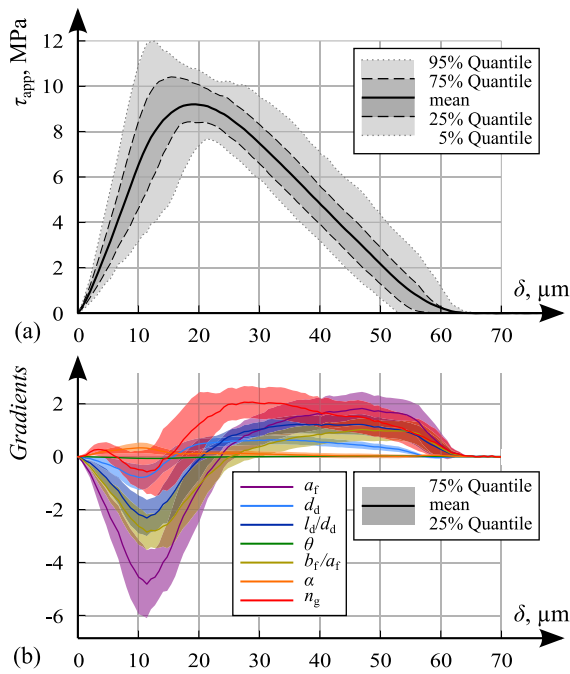


Fig. 8. (a) ANN-based shear stress–displacement predictions across the parameter space, showing the mean (solid black line), 25%–75% quantile band (interquartile range, dark gray), and 5%–95% quantile band (light gray). (b) Gradient analysis depicting the sensitivity of the predictions with respect to each input parameter.

reasonable, as a larger blade distance increases deformations through droplet plasticity, leading to greater overall deformations and effectively shifting the curve to the right, creating the appearance of a positive impact on $\hat{\tau}_{app}$.

3.2.3. Surrogate-based mechanical sensitivity analysis

To complement the geometrical analysis, this section investigates the influence of mechanical properties on interfacial failure in microdroplet tests. While keeping geometrical parameters constant, we vary key mechanical parameters, specifically those governing the interfacial traction–separation law and the frictional coefficients at the blade-droplet and fiber-droplet interfaces.

The fixed fiber-droplet geometry with circular cross-section is based on the flax-MAPP configuration reported by Pantaloni et al. (2021) (see Table 4). The normalized blade distance n_g was set to 0.15, corresponding to an actual blade distance $g = 42 \mu\text{m}$. Wide mechanical parameter ranges were chosen to capture the diverse compositions of biocomposites, see Table 4. The benchmark interface strength is based on the experimentally measured IFSS^{lit.} from Pantaloni et al. (2021), serving as a reference. The strength in normal direction, t_n , ranges from 0.1–1.5 · IFSS^{lit.}, while the shear strength t_s ranges from 0.5–2.0 · IFSS^{lit.}. The fracture energy G_n is set to 0.001–0.10 Nmm/mm², while G_s ranges from 0.01–0.50 Nmm/mm². Both Coulomb friction coefficients are varied up to 0.8. These six mechanical parameters define the input vector $\mathbf{x}_i \in \mathbb{I}^6$, following the same notation as in Section 2.3.2.

Similar to the geometrical study, 300 unique mechanical parameter sets were created using Latin hypercube sampling and subsequently simulated using FE analysis. As before, automatic and manual filtering of FE results is performed. Due to the extreme parameter combinations, 61 simulations had to be excluded. Most of these failed simulations struggled to fully capture post-peak behavior, which is inherently difficult to simulate using implicit FE solvers with the standard Newton scheme. After filtering, 192 samples were used for training and 47 for validation. The \mathcal{L}_{MAE} loss was 0.34 MPa for training and 0.36 MPa

for validation, indicating a sufficiently stable model to identify trends. Results remained consistent across different runs, reinforcing the robustness of the trained ANN. Fig. 9(a) illustrates the worst prediction among all validation samples.

The quantile bands in the shear stress–displacement ($\hat{\tau}_{app}$ - δ) diagram are analyzed first, see Fig. 9(b). Within the pre-peak regime up to displacements of roughly eight microns, all configurations behave similarly because elasto-plastic droplet and elastic fiber properties are constant throughout the study, and interfaces remain intact. Thereafter, the ranges of response significantly widen due to the large parameter ranges considered. The 5%–95% peak stress quantile ranges from roughly 6–16 MPa, and these wide bands continue in the post-peak regime, with ultimate displacements ranging from 20 to well over 100 μm . These large ranges in the microdroplet response result from the wide ranges of mechanical parameters considered (see Table 4).

Gradient-based sensitivity analysis is used to dive deeper into the relations between the mechanical parameters. The highest gradients within the mechanical parameters (Fig. 9(c)) are, unsurprisingly, associated with the shear direction parameters, as these represent the primary factors targeted in a microdroplet experiment. After the initial narrow bands, the spread in the droplet response widens significantly at around 10 μm of displacement. At first, the interfacial shear strength t_s drives this increase, as its gradient $\frac{\partial \hat{\tau}_{app}}{\partial t_s}$ increases first, see the blue line in Fig. 9(c). After most of the simulated droplets exhibited their corresponding peak shear stresses $\hat{\tau}_{app}$, the gradient related to t_s already decreases. This illustrates that the interfacial shear strength mainly increases the droplet shear strength, but has only a minor influence in the post-peak regime. At high displacements, beyond 50 μm , the gradient even turns negative, indicating that an increasing interfacial shear strength t_s decreases the droplet shear stress $\hat{\tau}_{app}$ at the same displacement.

In the post-peak regime, the interfacial shear fracture energy (G_s , in yellow) dominates the response of the droplet. The corresponding gradient $\frac{\partial \hat{\tau}_{app}}{\partial G_s}$ even exceeds the one related to the interfacial shear strength. Note that this is also related to the large range considered for this parameter, see Table 4. The gradient G_s increases very sharply once some simulated droplets have already peaked, at around 15 μm of displacement, and then continuously decreases.

The gradients related to the interface parameters in normal directions, t_n and G_n , quantify the sensitivity through mixed-mode interactions. While their magnitude is, as expected, significantly smaller compared to their shear counterparts, some interesting trends emerge: The gradient related to the normal traction (t_n , in magenta) increases much after the one related to shear and decreases significantly slower, highlighting that t_n also influences the post-peak response. The gradient related to the fracture energy in normal direction (G_n , in green) is very small throughout, despite the large range spanning two orders of magnitude.

Finally, the gradients related to shear coefficients (fiber-droplet interface friction μ_{intf} , in orange; blade friction μ_{blade} in red) are discussed. The interface friction gradient evolution peaks around the droplet's peak stress and continuously decreases in the post-peak regime. Notably, friction is activated right from the start—not just after debonding, explaining why the interface friction already influences the peak stress. The blade friction (μ_{blade} , in red) exhibits a negative gradient, with higher friction leading to slightly lower apparent shear strength. This can be explained by the additional normal tensile forces introduced near the interface at the blade height, where friction constrains the droplet.

While the gradient analysis of the full $\hat{\tau}_{app}$ - δ curve provides valuable insights, its interpretation is challenging due to nonlinear interactions and parameter interdependencies spread across the entire displacement range. In particular, it remains difficult to isolate how individual mechanical parameters influence specific features of the response, such as the maximum apparent shear stress $\tau_{app,max}$ or the displacement at peak stress. To disentangle these effects, an additional analysis was

Table 4
Variable mechanical and fixed geometrical parameters.

Mechanical Parameters						
t_n (MPa)	t_s (MPa)	G_n (Nmm/mm ²)	G_s (Nmm/mm ²)	μ_{blade} (-)	μ_{intf} (-)	
0.98–14.70	4.90–19.60	0.001–0.10	0.01–0.50	0–0.8	0–0.8	
Geometrical Parameters						
d_d^a (μm)	l_d/d_d^a (-)	a_t^a (μm)	θ^a ($^\circ$)	b/a_t (-)	α ($^\circ$)	n_s (-)
162	1.36	21	25.7	1.0	–	0.15

^a As reported by Pantaloni et al. (2021), Bellil et al. (2023).

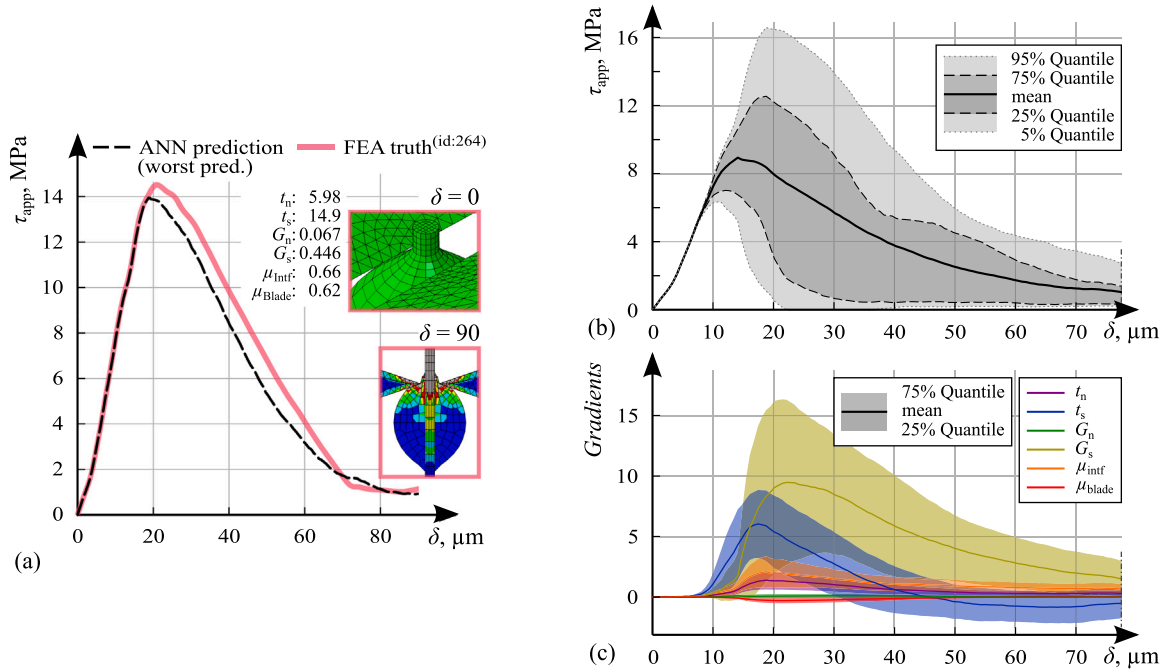


Fig. 9. ANN results of the mechanical parameter variations. (a) Worst prediction within the validation dataset. (b) Shear stress–displacement predictions across the parameter space, showing the mean (solid black line), 25%–75% quantile band (interquartile range, dark gray), and 5%–95% quantile band (light gray). (c) Gradient analysis depicting the sensitivity of the predictions with respect to each input parameter.

conducted by training a simplified ANN model focused exclusively on predicting the apparent shear strength $\hat{\tau}_{app,max}$. This model was trained using the same set of variable mechanical and fixed geometrical parameters listed in Table 4, ensuring a direct comparison with the full-curve predictions. Focusing on a scalar output allows for a more precise quantification of parameter influence through second-order derivatives.

The model follows the same fully connected feedforward architecture as the initial ANN but with reduced complexity. It consists of an input layer matching the number of variable mechanical parameters n , a single hidden layer with $4 \cdot n$ neurons, and an output layer predicting only the apparent strength $\hat{\tau}_{app,max}$ instead of the whole stress–displacement curve. To ensure smooth and differentiable outputs, the Continuously Differentiable Exponential Linear Unit (CELU) activation function was chosen, enabling second-order derivative computations for a more detailed sensitivity analysis. The sensitivity analysis is conducted at the center point of all normalized parameter intervals, ensuring equidistance from the parameter space boundaries and providing a representative basis for local interpretations. The model was trained using the Adam optimizer with a learning rate of 0.0001, a batch size of 4, and 1200 epochs. After training, the model achieved a coefficient of determination of $R^2 = 0.9513$ on the validation dataset when predicting $\hat{\tau}_{app,max}$.

For assessing the sensitivity of $\hat{\tau}_{app,max}$ with respect to the input parameters, again, the gradient information can be used. A first-order Taylor expansion, only including gradient information, resulted in an

$R^2 = 0.9683$ fit with respect to the exact prediction of the ANN. Incorporating second-order terms significantly improved the approximation to $R^2 = 0.9989$, suggesting that a model with first and second-order terms only can very accurately predict the shear strength.

The gradient analysis (Fig. 10(a)) provides first-order sensitivities, revealing how strongly each individual mechanical parameter influences the apparent shear strength $\hat{\tau}_{app,max}$. The highest positive gradient is, by design of the microdroplet test, associated with the interfacial shear strength t_s . In contrast, the shear fracture energy G_s has a much smaller influence.

While first-order gradients quantify the sensitivity regarding changes in a single parameter, they do not capture interactions between parameters. The Hessian analysis (Fig. 10(b)) provides second-order sensitivities, revealing nonlinear couplings between mechanical parameters. Diagonal elements in the Hessian ($\frac{\partial^2 \hat{\tau}_{app,max}}{\partial x_i^2}$) represent the second derivative of $\hat{\tau}_{app,max}$ with respect to the same parameter. For example, the negative diagonal value $\frac{\partial^2 \hat{\tau}_{app,max}}{\partial t_s^2} \approx -6$ indicates that increasing t_s reduces its own sensitivity—meaning at higher values, further increasing shear traction has less impact on $\hat{\tau}_{app,max}$. This suggests a cap, where additional traction no longer leads to a significant increase in apparent shear strength. This corresponds to the trend in Fig. 9(b): While the 5% quantile reaches a maximum at approximately 5 MPa, the 95% quantile peaks just above 16 MPa, despite the input range of t_s spanning 4.90–19.60 MPa. This further confirms that increasing t_s

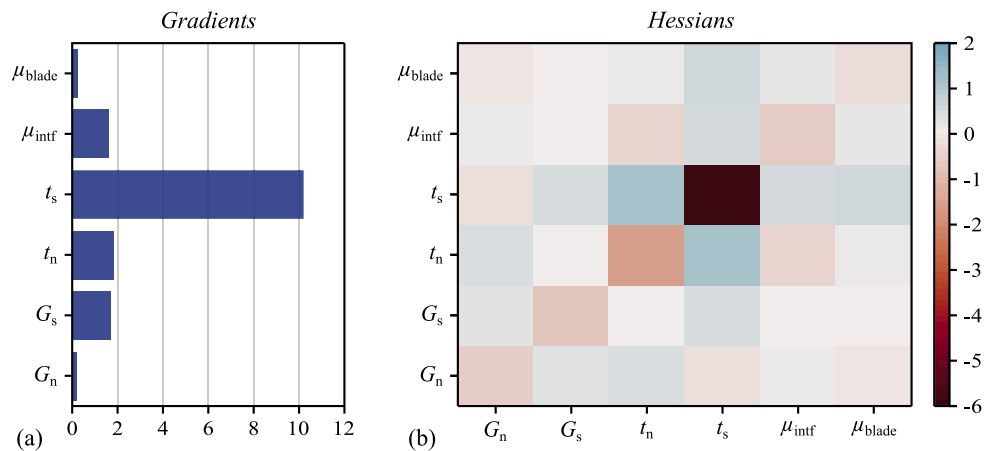


Fig. 10. Sensitivity analysis of the ANN trained on apparent shear strength $\hat{\tau}_{app,max}$ with respect to the mechanical input parameters: (a) Gradient analysis showing first-order sensitivities, and (b) Hessian analysis illustrating second-order sensitivities, highlighting parameter interactions.

beyond a certain point has diminishing benefits on the apparent shear strength.

Off-diagonal elements ($\frac{\partial^2 \hat{\tau}_{app,max}}{\partial x_i \partial x_k}$) describe how two different parameters interact—whether their effects are independent or coupled. Strong positive values ($\frac{\partial^2 \hat{\tau}_{app,max}}{\partial x_i \partial x_k} > 0$) indicate that the two parameters reinforce each other, meaning increasing one enhances the effect of the other. Strong negative values ($\frac{\partial^2 \hat{\tau}_{app,max}}{\partial x_i \partial x_k} < 0$) suggest that the parameters compete, so increasing one reduces the effect of the other. If $\frac{\partial^2 \hat{\tau}_{app,max}}{\partial x_i \partial x_k} \approx 0$, the parameters act independently, with little to no interaction. For example, $\frac{\partial^2 \hat{\tau}_{app,max}}{\partial t_n \partial t_s} \approx +2$ suggest that increasing t_s increases the sensitivity of t_n . In a mixed-mode model, this is expected. Increasing the limiting stress of one failure mode results in a shift to the other failure mode. Therefore, the maximum apparent shear strength $\hat{\tau}_{app,max}$ becomes more sensitive to the failure mode with increasing dominance.

4. Conclusion & outlook

This study introduced a new approach for extracting the constitutive behavior of fiber–matrix interfaces in biocomposites from microdroplet tests by means of finite element simulations. By systematically varying both mechanical and geometrical parameters in a high-fidelity modeling framework and training surrogate neural networks on the resulting dataset, we gained detailed insights into parameter sensitivities and interactions. In particular, the results highlight how strongly geometrical variability in the investigated microdroplet system can affect the apparent interfacial shear strength for the studied flax–polypropylene biocomposites, and how the applied traction–separation law with potentially mixed-mode coupling exerts a dominant role—beyond what is captured by scalar strength measures like the IFSS.

Looking forward, the integration of surrogate models such as ANNs offers promising potential for inverse identification of interfacial properties. Provided that sufficiently detailed experimental data becomes available – including force–displacement responses paired with accurate droplet and fiber geometries – optimization algorithms could be used to recover reliable parameter sets efficiently. Once trained, such surrogate models could replace the tedious finite element-based fitting loop entirely, yielding the essential interface parameters, such as interface strength and fracture energy. In future experimental campaigns, this would allow researchers to directly back-calculate full interfacial parameter sets from microdroplet tests—making use of each test to its full extent and facilitating consistent upscaling to composite-level predictions. Ongoing research, as detailed in Senk (2025), already

demonstrates the potential of using these identified laws within composite scale models to accurately predict the non-linear failure behavior of sustainable biocomposites.

CRedit authorship contribution statement

Valentin Senk: Writing – review & editing, Writing – original draft, Visualization, Validation, Methodology, Investigation, Data curation, Conceptualization. **Markus Königsberger:** Writing – review & editing, Validation, Supervision, Investigation, Conceptualization. **Sebastian Pech:** Software, Resources, Methodology, Conceptualization. **Josef Füssl:** Supervision, Project administration, Funding acquisition, Conceptualization.

Declaration of competing interest

The authors declare that they have no known competing financial interests or personal relationships that could have appeared to influence the work reported in this paper.

Acknowledgments

This research was funded in whole or in part by the Austrian Science Fund (FWF), Austria [10.55776/F77, 10.55776/Y1093]. For open access purposes, the authors have applied a CC BY public copyright license to any accepted manuscript version arising from this submission. The authors also gratefully acknowledge TU Wien Bibliothek, Austria for financial support through its Open Access Funding Program.

The authors thank the HORIZON AI-TRANSPWOOD (AI-Driven Multiscale Methodology to Develop Transparent Wood as Sustainable Functional Material) project, Grant no. 101138191, co-funded by the European Union. Views and opinions expressed are, however, those of the author(s) only and do not necessarily reflect those of the European Union or HaDEA. Neither the European Union nor the granting authority can be held responsible for them.

Furthermore, the financial support from the Austrian Federal Ministry of Labour and Economy, Austria, the National Foundation for Research, Technology and Development, Austria, and the Christian Doppler Research Association, Austria is gratefully acknowledged.

Data availability

Data will be made available on request.

References

- Abaqus, 2024. *Abaqus 2024: Software*. Dassault Systèmes Simulia Corp, Rhode Island, United States.
- Ahmadian, Hossein, Yang, Ming, Nagarajan, Anand, Soghrati, Soheil, 2019. Effects of shape and misalignment of fibers on the failure response of carbon fiber reinforced polymers. *Comput. Mech.* (ISSN: 01787675) 63 (5), 999–1017. <http://dx.doi.org/10.1007/s00466-018-1634-1>.
- Ash, J.T., Cross, W.M., Svalstad, D., Kellar, J.J., Kjerengtroen, L., 2003. Finite element evaluation of the microbond test: meniscus effect, interphase region, and vise angle. *Compos. Sci. Technol.* (ISSN: 0266-3538) 63 (5), 641–651. [http://dx.doi.org/10.1016/S0266-3538\(02\)00256-7](http://dx.doi.org/10.1016/S0266-3538(02)00256-7).
- Baley, Christophe, Gomina, Moussa, Breard, Joel, Bourmaud, Alain, Davies, Peter, 2020. Variability of mechanical properties of flax fibres for composite reinforcement. *A review. Ind. Crop. Prod.* (ISSN: 0926-6690) 145, 111984. <http://dx.doi.org/10.1016/j.indcrop.2019.111984>.
- Bannister, D.J., Andrews, M.C., Cervenka, A.J., Young, R.J., 1995. Analysis of the single-fibre pull-out test by means of Raman spectroscopy: Part II. Micromechanics of deformation for an aramid/epoxy system. *Compos. Sci. Technol.* (ISSN: 0266-3538) 53 (4), 411–421. [http://dx.doi.org/10.1016/0266-3538\(95\)00030-5](http://dx.doi.org/10.1016/0266-3538(95)00030-5).
- Bellil, Shaima, Pantaloni, Delphin, Shah, Darshil U., Duigou, Antoine Le, Baley, Christophe, Beaugrand, Johnny, Bourmaud, Alain, Guessasma, Sofiane, 2023. Prediction of interfacial behaviour of single flax fibre bonded to various matrices by simulation of microdroplet test. *Compos. Part C: Open Access* (ISSN: 2666-6820) 11, 100351. <http://dx.doi.org/10.1016/j.jcomc.2023.100351>.
- Bourmaud, A., Ausias, G., Lebrun, G., Tachon, M.-L., Baley, C., 2013. Observation of the structure of a composite polypropylene/flax and damage mechanisms under stress. *Ind. Crop. Prod.* (ISSN: 0926-6690) 43, 225–236. <http://dx.doi.org/10.1016/j.indcrop.2012.07.030>.
- Camanho, Pedro P., Davila, Carlos G., 2002. *Mixed-Mode Decohesion Finite Elements for the Simulation of Delamination in Composite Materials*. Technical Report NASA/TM-2002-211737, NASA Langley Research Center.
- Carroll, B.J., 1976. The accurate measurement of contact angle, Phase Contact Areas, drop volume, and Laplace excess pressure in drop-on-fiber systems. *J. Colloid Interface Sci.* 57 (3), 488–495. [http://dx.doi.org/10.1016/0021-9797\(76\)90227-7](http://dx.doi.org/10.1016/0021-9797(76)90227-7).
- Chou, C.T., Gaur, U., Miller, B., 1994. The effect of microvise gap width on microbond pull-out test results. *Compos. Sci. Technol.* (ISSN: 0266-3538) 51 (1), 111–116. [http://dx.doi.org/10.1016/0266-3538\(94\)90161-9](http://dx.doi.org/10.1016/0266-3538(94)90161-9).
- Craven, J.P., Cripps, R., Viney, C., 2000. Evaluating the silk/epoxy interface by means of the microbond test. *Compos. Part A: Appl. Sci. Manuf.* (ISSN: 1359-835X) 31 (7), 653–660. [http://dx.doi.org/10.1016/S1359-835X\(00\)00042-7](http://dx.doi.org/10.1016/S1359-835X(00)00042-7).
- Dsouza, R., Antunes, P., Kakkonen, M., Jokinen, J., Sarlin, E., Kallio, P., Kanerva, M., 2020. 3D interfacial debonding during microbond testing: Advantages of local strain recording. *Compos. Sci. Technol.* (ISSN: 0266-3538) 195, 108163. <http://dx.doi.org/10.1016/j.compscitech.2020.108163>.
- Dsouza, Royson Donate, Di Vito, Donato, Jokinen, Jarno, Kanerva, Mikko, 2023. Mutual dependence of experimental and data analysis features in characterization of fiber-matrix interface via microdroplets. *Polym. Compos.* 44 (11), 7611–7630. <http://dx.doi.org/10.1002/pc.27649>.
- Dzenis, Yuri A., Qian, Jiang, 2001. Analysis of microdamage evolution histories in composites. *Int. J. Solids Struct.* 38 (10–13), 1831–1854. [http://dx.doi.org/10.1016/S0020-7683\(00\)00130-0](http://dx.doi.org/10.1016/S0020-7683(00)00130-0).
- Hampe, A., Marotzke, C., 1997. The energy release rate of the fiber/polymer matrix interface: Measurement and theoretical analysis. *J. Reinf. Plast. Compos.* 16 (4), 341–352. <http://dx.doi.org/10.1177/073168449701600405>.
- Herrera-Franco, P.J., Drzal, L.T., 1992. Comparison of methods for the measurement of fibre/matrix adhesion in composites. *Composites* (ISSN: 0010-4361) 23 (1), 2–27. [http://dx.doi.org/10.1016/0010-4361\(92\)90282-Y](http://dx.doi.org/10.1016/0010-4361(92)90282-Y).
- Herrera-Franco, Pedro J., Rao, Venkatesh, Drzal, Lawrence T., Chiang, Martin Y.M., 1992. Bond strength measurement in composites: Analysis of experimental techniques. *Compos. Eng.* 2 (1), 31–45. [http://dx.doi.org/10.1016/0961-9526\(92\)90016-Y](http://dx.doi.org/10.1016/0961-9526(92)90016-Y).
- Huang, Silu, Fu, Qiuni, Yan, Libo, Kasal, Bohumil, 2021. Characterization of interfacial properties between fibre and polymer matrix in composite materials – A critical review. *J. Mater. Res. Technol.* (ISSN: 2238-7854) 13, 1441–1484. <http://dx.doi.org/10.1016/j.jmrt.2021.05.076>.
- Iman, Ronald L., Conover, W.J., 1980. Small sample sensitivity analysis techniques for computer models with an application to risk assessment. *Comm. Statist. Theory Methods* 9 (17), 1749–1842. <http://dx.doi.org/10.1080/03610928008827996>.
- Innes, Michael, 2018. Flux: Elegant machine learning with julia. *J. Open Source Softw.* <http://dx.doi.org/10.21105/joss.00602>.
- Innes, Michael, Saba, Elliot, Fischer, Keno, Gandhi, Dhairya, Rudilosso, Marco Concetto, Joy, Neethu Mariya, Karmali, Tejan, Pal, Avik, Shah, Viral, 2018. Fashionable modelling with flux. *CoRR abs/1811.01457*, URL <https://arxiv.org/abs/1811.01457>.
- Kang, Soo-Keun, Lee, Deok-Bo, Choi, Nak-Sam, 2009. Fiber/epoxy interfacial shear strength measured by the microdroplet test. *Compos. Sci. Technol.* (ISSN: 0266-3538) 69 (2), 245–251. <http://dx.doi.org/10.1016/j.compscitech.2008.10.016>.
- Kim, Jang-Kyo, Mai, Yiu-Wing, 1991. High strength, high fracture toughness fibre composites with interface control—A review. *Compos. Sci. Technol.* 41, 333–378. [http://dx.doi.org/10.1016/0266-3538\(91\)90072-W](http://dx.doi.org/10.1016/0266-3538(91)90072-W).
- Königsberger, Markus, Lukacevic, Markus, Füssli, Josef, 2023. Multiscale micromechanics modeling of plant fibers: upscaling of stiffness and elastic limits from cellulose nanofibrils to technical fibers. *Mater. Struct.* 56 (13), <http://dx.doi.org/10.1617/s11527-022-02097-2>.
- Laurikainen, P., Kakkonen, M., von Essen, M., Tanhuanpää, O., Kallio, P., Sarlin, E., 2020. Identification and compensation of error sources in the microbond test utilising a reliable high-throughput device. *Compos. Part A: Appl. Sci. Manuf.* (ISSN: 1359-835X) 137, 105988. <http://dx.doi.org/10.1016/j.compositesa.2020.105988>.
- Li, Dan, Yang, Qing-Sheng, Liu, Xia, He, Xiao-Qiao, 2017. Experimental and cohesive finite element investigation of interfacial behavior of CNT fiber-reinforced composites. *Compos. Part A: Appl. Sci. Manuf.* (ISSN: 1359-835X) 101, 318–325. <http://dx.doi.org/10.1016/j.compositesa.2017.06.033>.
- McKay, M.D., Beckman, R.J., Conover, W.J., 1979. A comparison of three methods for selecting values of input variables in the analysis of output from a computer code. *Technometrics* 21 (2), 239–245.
- Miller, Bernard, Muri, Pierre, Rebenfeld, Ludwig, 1987. A microbond method for determination of the shear strength of a fiber/resin interface. *Compos. Sci. Technol.* (ISSN: 0266-3538) 28 (1), 17–32. [http://dx.doi.org/10.1016/0266-3538\(87\)90059-5](http://dx.doi.org/10.1016/0266-3538(87)90059-5).
- Minnicino, Michael A., Santare, Michael H., 2012. Modeling the progressive damage of the microdroplet test using contact surfaces with cohesive behavior. *Compos. Sci. Technol.* (ISSN: 0266-3538) 72 (16), 2024–2031. <http://dx.doi.org/10.1016/j.compscitech.2012.09.009>.
- Nian, Guodong, Li, Qiyang, Xu, Qiang, Qu, Shaoxing, 2018. A cohesive zone model incorporating a Coulomb friction law for fiber-reinforced composites. *Compos. Sci. Technol.* (ISSN: 0266-3538) 157, 195–201. <http://dx.doi.org/10.1016/j.compscitech.2018.01.037>.
- Pandey, Gajendra, Kareliya, Chirag H., Singh, Raman P., 2012. A study of the effect of experimental test parameters on data scatter in microbond testing. *J. Compos. Mater.* 46 (3), 275–284. <http://dx.doi.org/10.1177/0021998311410508>.
- Pantaloni, Delphin, Rudolph, Anton Loïc, Shah, Darshil U., Baley, Christophe, Bourmaud, Alain, 2021. Interfacial and mechanical characterization of biodegradable polymer-flax fibre composites. *Compos. Sci. Technol.* (ISSN: 0266-3538) 201, 108529. <http://dx.doi.org/10.1016/j.compscitech.2020.108529>.
- Pisanova, E., Zhandarov, S., Mäder, E., Ahmad, I., Young, R.J., 2001. Three techniques of interfacial bond strength estimation from direct observation of crack initiation and propagation in polymer–fibre systems. *Compos. Part A: Appl. Sci. Manuf.* (ISSN: 1359-835X) 32 (3), 435–443. [http://dx.doi.org/10.1016/S1359-835X\(00\)00054-3](http://dx.doi.org/10.1016/S1359-835X(00)00054-3).
- Sato, Mio, Imai, Erina, Koyanagi, Jun, Ishida, Yuichi, Ogasawara, Toshio, 2017. Evaluation of the interfacial strength of carbon-fiber-reinforced temperature-resistant polymer composites by the micro-droplet test. *Adv. Compos. Mater.* <http://dx.doi.org/10.1080/09243046.2017.1284638>.
- Savitzky, Abraham, Golay, Marcel J.E., 1964. Smoothing and differentiation of data by simplified least squares procedures. *Anal. Chem.* 36 (8), 1627–1639. <http://dx.doi.org/10.1021/ac60214a047>.
- Schüller, T., Bahr, U., Beckert, W., Lauke, B., 1998. Fracture mechanics analysis of the microbond test. *Compos. Part A: Appl. Sci. Manuf.* (ISSN: 1359-835X) 29 (9), 1083–1089. [http://dx.doi.org/10.1016/S1359-835X\(98\)00044-X](http://dx.doi.org/10.1016/S1359-835X(98)00044-X).
- Senk, Valentin, 2025. *Mechanics of Plant Fiber-Reinforced Composite Materials: from Micro-Meso Modeling to Interactive Frameworks for Material-Informed Design in Early Planning Phases* (Ph.D. thesis). TU Wien, Vienna, Austria, <http://dx.doi.org/10.34726/hss.2025.138401>.
- Senk, Valentin, Königsberger, Markus, Pech, Sebastian, Lukacevic, Markus, Schwaighofer, Michael, Zelaya-Lainez, Luis, Füssli, Josef, 2025. Numerical modeling of plant fiber-reinforced composites: Predicting macroscopic strength and nonlinear behavior through fiber, matrix, and interface failure. *Mech. Mater.* (ISSN: 0167-6636) 205, 105318. <http://dx.doi.org/10.1016/j.mechmat.2025.105318>.
- Shu, Wenya, Stanculescu, Ilinca, 2023. Computational modeling and multiscale homogenization of short fiber composites considering complex microstructure and imperfect interfaces. *Compos. Struct.* (ISSN: 0263-8223) 306, 116592. <http://dx.doi.org/10.1016/j.compstruct.2022.116592>.
- Sockalingam, Subramani, Dey, Moutushi, Gillespie, John W., Keefe, Michael, 2014. Finite element analysis of the microdroplet test method using cohesive zone model of the fiber/matrix interface. *Compos. Part A: Appl. Sci. Manuf.* (ISSN: 1359-835X) 56, 239–247. <http://dx.doi.org/10.1016/j.compositesa.2013.10.021>.
- Song, Bihai, Bismarck, Alexander, Tahhan, Ralf, Springer, Jürgen, 1998. A generalized drop length–height method for determination of contact angle in drop-on-fiber systems. *J. Colloid Interface Sci.* (ISSN: 0021-9797) 197 (1), 68–77. <http://dx.doi.org/10.1006/jcis.1997.5218>.
- Thomason, James, Carlin, Andrew, Yang, Liu, 2024. Non-circular cross-section fibres for composite reinforcement—A review with a focus on flat glass fibres. *Fibers* 12 (11), <http://dx.doi.org/10.3390/fib12110098>.
- Urquhart, Magnus, Ljungskog, Emil, Sebben, Simone, 2020. Surrogate-based optimisation using adaptively scaled radial basis functions. *Appl. Soft Comput.* (ISSN: 1568-4946) 88, 106050. <http://dx.doi.org/10.1016/j.asoc.2019.106050>.

- Vida, Christoffer, Lukacevic, Markus, Eberhardsteiner, Josef, Füssl, Josef, 2022. Modeling approach to estimate the bending strength and failure mechanisms of glued laminated timber beams. *Eng. Struct.* (ISSN: 0141-0296) 255, 113862. <http://dx.doi.org/10.1016/j.engstruct.2022.113862>.
- Vida, Christoffer, Lukacevic, Markus, Hochreiner, Georg, Füssl, Josef, 2023. Size effect on bending strength of glued laminated timber predicted by a numerical simulation concept including discrete cracking. *Mater. Des.* (ISSN: 0264-1275) 225, 111550. <http://dx.doi.org/10.1016/j.matdes.2022.111550>.
- Wagner, H.D., Gallis, H.E., Wiesel, E., 1993. Study of the interface in kevlar 49-epoxy composites by means of microbond and fragmentation tests: effects of materials and testing variables. *J. Mater. Sci.* 28, 2238–2244. <http://dx.doi.org/10.1007/BF00367590>.
- Zhao, Q., Qian, C.C., Harper, L.T., Warrior, N.A., 2018. Finite element study of the microdroplet test for interfacial shear strength: Effects of geometric parameters for a carbon fibre/epoxy system. *J. Compos. Mater.* 52 (16), 2163–2177. <http://dx.doi.org/10.1177/0021998317740943>.
- Zhi, Chao, Long, Hairu, Miao, Menghe, 2017. Influence of microbond test parameters on interfacial shear strength of fiber reinforced polymer-matrix composites. *Compos. Part A: Appl. Sci. Manuf.* (ISSN: 1359-835X) 100, 55–63. <http://dx.doi.org/10.1016/j.compositesa.2017.05.004>.